Article

Design, Fabrication and Validation of Mixed Order Distributed Feed-Back Organic Diode Laser Cavity

Amani Ouirimi [1,2,*], Alex Chamberlain Chime [1,2,3], Nixson Loganathan [1,2], Mahmoud Chakaroun [1,2], Daan Lenstra [4] and Alexis P. A. Fischer [1,2]

1 Laboratoire de Physique des Lasers, Université Sorbonne Paris Nord, UMR CNRS 7538, 99 Avenue JB Clément, 93430 Villetaneuse, France; alexchamberlain.chime@univ-paris13.fr (A.C.C.); nixson.loganathan@univ-paris13.fr (N.L.); chakaroun@univ-paris13.fr (M.C.); fischer@univ-paris13.fr (A.P.A.F.)
2 Centrale de Proximité en Nanotechnologies de Paris Nord, Université Sorbonne Paris Nord, 99 Avenue JB Clément, 93430 Villetaneuse, France
3 IUT-FV, Université de Dschang, P.O. Box 134 Bandjoun, Cameroon
4 Institute of Photonics Integration, Eindhoven University of Technology, P.O. Box 513, 5600 MB Eindhoven, The Netherlands; dlenstra@tue.nl
* Correspondence: amani.ouirimi@univ-paris13.fr

Abstract: In the context of the quest for the organic laser diode, we address a key challenge to design and fabricate high-quality factor cavities compatible with electrical excitation of organic semiconductors. More precisely, we present the design of DFB micro-cavities for integration in organic laser diodes and their validation under optical pumping. To design high-quality factor mixed-order DFB micro-cavities, we consider the half- and quarter-wavelength multilayered system and use the optical waveguide analysis to quantify the effective indices of the high and low indices, and the matrix transfer method to calculate the reflectances. Matrices of DFB micro-cavities made from different doses and different grating periods were fabricated. We then identified those showing laser emission under optical pumping as an indication of optimal matching of their resonance wavelength with respect to the electroluminescence peak of the organic gain material. Potential applications of organic laser diodes deal with light communication, spectroscopy, sensors, and other applications where heterogenous integration is important.

Keywords: optoelectronics; photonic; OLED; DFB cavities; organic laser diode

1. Introduction

In the field of organic optoelectronics, several devices have been demonstrated, such as the organic light-emitting diode (OLED) [1], organic photovoltaic (OPV) [2] and organic photodetector (OPD) [3]. The only device yet to be demonstrated unambiguously is the organic laser diode (OLD), which would constitute a disruptive alternative to conventional laser diodes by signifying a credible and original low-tech organic photonic platform [4]. A key challenge in organic optoelectronics is achieving electrically excited lasing with an organic heterostructure. However, this has not yet been demonstrated due to factors such as the need for high-quality cavity design and fabrication compatible with intense electrical excitation.

The quest for the organic laser diode is part of a scientific evolution that began with liquid laser dyes in the 1960s and continues with optically pumped organic solid lasers. The electrical excitation of organic semiconductors that are also laser gain media then becomes the missing link in the history of organic lasers. Organic thin-film lasers are compact sources that have great potential for numerous applications, such as spectroscopy, pollutant detection, telecommunications, and sensors [1,5]. The library of organic semiconductors is almost infinite and covers the entire visible spectrum, contrary to their inorganic counterparts which offer a limited number of bandgaps. Organic semiconductor physics is based

on polarons and Frenkel excitons, whereas Wanier excitons hardly play a role compared to the holes and electrons at the heart of the inorganic semiconductor physics. Compared to conventional crystal semiconductors used in laser diodes, which require epitaxy under ultra-high vacuum, organic semiconductors are amorphous, can be thermally evaporated under a vacuum typically at 200 °C.

Thanks to the amorphous properties of OSCs, their heterogeneous integration into the silicon CMOS circuit is very easy, at least compared to the epitaxial growth and lattice mismatch problems of the GaN crystals on silicon [6,7]. Hence, their ability to emit coherent light over a wide range of the visible spectrum, coupled with their simple and low-cost manufacturing techniques (printing, roll-to-roll, self-assembly, and soft-lithography), make them potential competitors to existing tunable visible sources. The most promising applications will be where heterogeneous integration will give them a technical advantage over their inorganic counterparts. Consequently, the development of an organic laser diode will pave the way for future advancements in simple and cost-effective laser technology, enabling the realization of a monolithic optical platform with a lower carbon footprint based on organic semiconductors. The differences between the different types of lasers are summarized in Table 1.

Table 1. Comparison of the different laser technologies.

Dye laser	Organic solid-state laser	Organic laser diode	Conventional laser diode
Liquid state	Amorphous thin film (Solid state)	Amorphous thin film (Solid state)	Crystalline thin film
Optically pumped	Optically pumped	Electrical excitation	Electrical excitation
No heterogeneous integration	Relatively easy heterogenous integration thanks to the amorphous state	Easy heterogenous integration including on silicon thanks to the amorphous state Environmentally friendly fabrication process—Short fabrication time Fabrication steps ~30	Difficult heterogenous integration due to lattice mismatch Often toxic materials Long fabrication time Fabrication steps ~300
Macroscopic device		Microscopic device	Microscopic device
Frenkel excitons (binding energy ~1 eV, radius 1 nm) [8]	Frenkel excitons (binding energy ~1 eV, radius 1 nm) [8]	Polarons and Frenkel excitons (binding energy ~1 eV, radius 1 nm) [8]	Wanier excitons Irrelevant at room temperature

The demonstration of the OLD requires the integration of a high-quality factor microcavity into an organic hetero-structure sandwiched between electrodes. From the literature, the cavity type offering the lowest laser threshold under optical pumping is the mixed-order distributed feedback (DFB) [9–13].

In 2019, promising indications have been reported by the Adachi group with a device implementing a DFB mixed-order cavity and using a bicarbazole dye named BsB-Cz [14]. Confirmation by other groups is still pending. The results obtained remain under debate because of the surprisingly low laser threshold (0.5 kA/cm^2) due to the absence of any mention of the cavity quality factor and the incomplete rationalization of the low triplet absorption of the BsB-Cz dye. These illustrate the remaining efforts to demonstrate the OLD in a reproducible manner [15]. Another question remains: How is the resonance frequency of the cavity matched accurately with the peak of electroluminescence of the gain material, despite uncertainties on the indices and the limiting resolution of the DFB micro-cavity fabrication method?

In the current study, we present the design of the DFB micro-cavities and its validation under optical pumping.

2. Laser Cavity Design

The consensus in the literature to obtain an OLD is to combine an OLED with a mixed-order DFB micro-cavity. This type of cavity consists of three sections: two first-order gratings separated by a second-order grating, in which the first-order gratings act as mirrors providing the confinement of light, and the second-order grating allows for the out-coupling of the light perpendicularly to the cavity [9].

Our method to integrate the micro-cavity into the OLED is to pattern the DFB grating directly with low-index insulating lines on top of the transparent and conductive anodes.

Such a distributed feedback micro-cavity is schematized in Figure 1a. The first-order sections consist of the periodical alternation of M low-index n_L quarter-wavelength lines of width $\Lambda_L = \frac{\lambda}{4n_L}$ spaced by $\Lambda_H = \frac{\lambda}{4n_H}$, where n_L and n_H are the effective refractive index of the different stacks shown in Figure 1b (stack 1) and Figure 1c (stack 2), respectively.
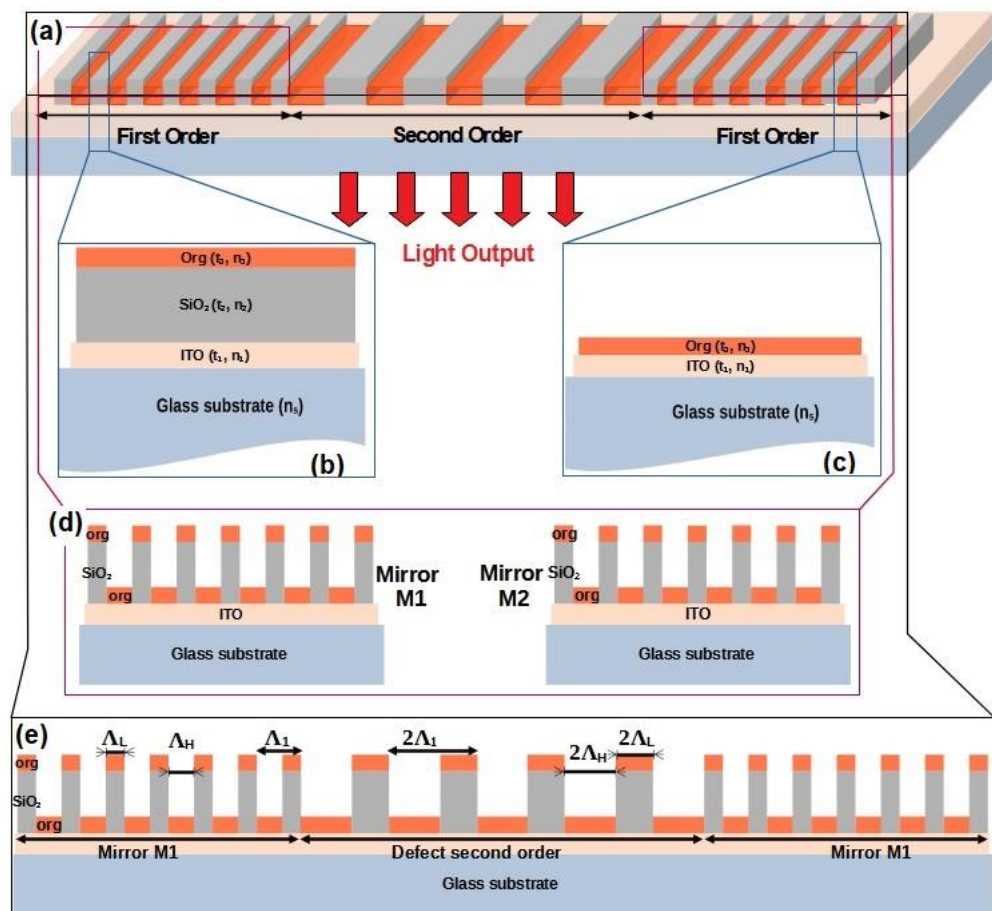

Figure 1. Mixed-order DFB cavity: (**a**) DFB structure with periodic SiO$_2$ layer as both insulating and low-index material, (**b**) Detail of the type 1 section with the SiO$_2$ layer resulting in low effective index nL, (**c**) Detail of the type 2 section without the SiO$_2$ layer resulting in a high effective index nL, (**d**) DFB mirrors and multilayered waveguide, (**e**) Detailed structure of a DFB cavity with mirrors and defects.

Stack 1 consists of a glass substrate covered with a transparent and conductive anode (Indium Tin Oxide: ITO) with refractive index n_1 and thickness t_1, an insulating layer (SiO$_2$) with refractive index n_2 and thickness t_2, and ends with an organic layer with refractive index n_3 and thickness t_3. The superstrate is air with refractive index n_0. Stack 2 consists of the same glass substrate covered with ITO (n_1, t_1) and ends with the organic layers (n_3, t_3). The superstrate is air. Depending on the thicknesses t_1, t_2 and t_3, the effective indices n_H and n_L may vary. The second-order section consists of periodical alternation of D low-index n_L half-wavelength lines of width $2\Lambda_L$ spaced by $2\Lambda_H$.

The geometry of the device is fully defined with the set $\{t_1, t_2, t_3, \Lambda_H, \Lambda_L, M$ and $D\}$. The scientific approach to define these parameters is divided into four parts. Firstly, the ITO and organic layers thicknesses (t_1 and t_3) are defined using the optimization of the confinement factor as a first criterium (Section 2.1.1). Secondly, the SiO_2 thickness (t_2) is defined using the enhancement of the effective index contrast $\Delta_{neff} = n_H - n_L$ as a criterium necessary to maximize the micro-cavity quality factors (Section 2.1.2). Once t_1, t_2 and t_3 are defined, the effective indices are fixed and can be used to calculate the quarter wavelength line widths Λ_H and Λ_L, as presented in Section 2.2.1. Finally, M is chosen so as to target a quality factor above 1000. This approach is presented in Section 2.2.2.

2.1. Optical Waveguide

The first optimization criterium concerns the confinement factor Γ, i.e., the fraction of the optical field within the organic layer, while the second optimization criterium deals with the optimal effective index contrast Δ_{neff} (Equation (1))

$$\Delta_{neff} = n_H - n_L \tag{1}$$

They are calculated using a 1-D mode solver for optical dielectric multi-layer slab waveguides [16].

This applet solves the Helmholtz equation and calculates the effective indices of guided modes and the corresponding optical fields from which the confinement factor Γ and the index contrast Δ_{neff} are calculated for the different TE and TM modes.

2.1.1. Confinement Factor

The confinement factor Γ is investigated first as a function of t_1 the ITO layer thickness and second as a function of t_3 the organic layer thicknesses.

To identify the optimal thickness of the ITO layer, we focus on the first TE mode (TE_0), disregarding the TM mode. Figure 2 shows the confinement factor Γ as a function of t_1 for a fixed typical OLED organic layer thickness $t_3 = 125$ nm. A clear maximum is observed at $\Gamma = 0.31$ for 50 nm $\leq t_1 \leq 55$ nm. Such ITO thicknesses are much thinner than what is usually considered for conventional OLEDs; commercially available glass substrates covered with $5\,\Omega/sq$ and $15\,\Omega/sq$ ITO layers correspond to 140 nm and 340 nm ITO layer thicknesses.

Figure 3 presents from left to right Γ, the confinement factor as a function of t_3 the organic layer thickness for different TE and TM modes and for three different ITO layer thicknesses, $t_1 = 50$ nm, the optimal value identified in the previous study, $t_1 = 140$ nm, and $t_1 = 340$ nm, the commercially available ITO layers. For large values of t_3 several modes arise: from left to right, TE modes appear in green, black, and red, while TM modes appear in magenta, cyan, and blue. The different mode orders TX_0, TX_1, TX_2, TX_3 are plotted in solid lines, dashed lines, dotted lines, and dash-dotted lines, respectively.

In the 50 nm thick ITO layer case, the TE_0 and TM_0 modes coexist up to an organic layer thickness $t_3 = 400$ nm, where the TE_1 appears. TM_1, TE_2, and TM_2 appear at $t_3 = 450$ nm, $t_3 = 750$ nm, $t_3 = 800$ nm, respectively. In this 50 nm case, the design is more favorable, with an organic layer thickness below 400 nm, as this will limit the number of modes. For this thickness, the confinement factors reach $\Gamma = 0.8$ for TE_0 and $\Gamma = 0.83$ for TM_0.

A similar reasoning applied to the 140 nm thick ITO layer case leads to confinement factors $\Gamma = 0.40$ for TE_0 and $\Gamma = 0.49$ for TM_0 for an organic layer thickness $t_3 = 275$ nm, defined by the emergence of the TE_1 mode. Note that for the same organic layer thickness $t_3 = 400$ nm the confinement factors are $\Gamma = 0.47$ and 0.56 for TE_0 and TM_0 modes, respectively, which is much lower than what was estimated in the 50 nm ITO layer thickness case.

For the 340 nm thick ITO layer case, the TE_1 (TM_1) coexists with TE_0 (TM_0) even without the organic layer ($t_3 = 0$ nm). Obviously, this is because with an ITO layer thickness of 340 nm, TE_1 (TM_1) already coexists with TE_0 (TM_0). The confinement factors

saturate at $\Gamma = 0.12$ and 0.16 for the TE_0 and TM_0 modes, respectively, which is much lower than what was estimated in the previous cases.
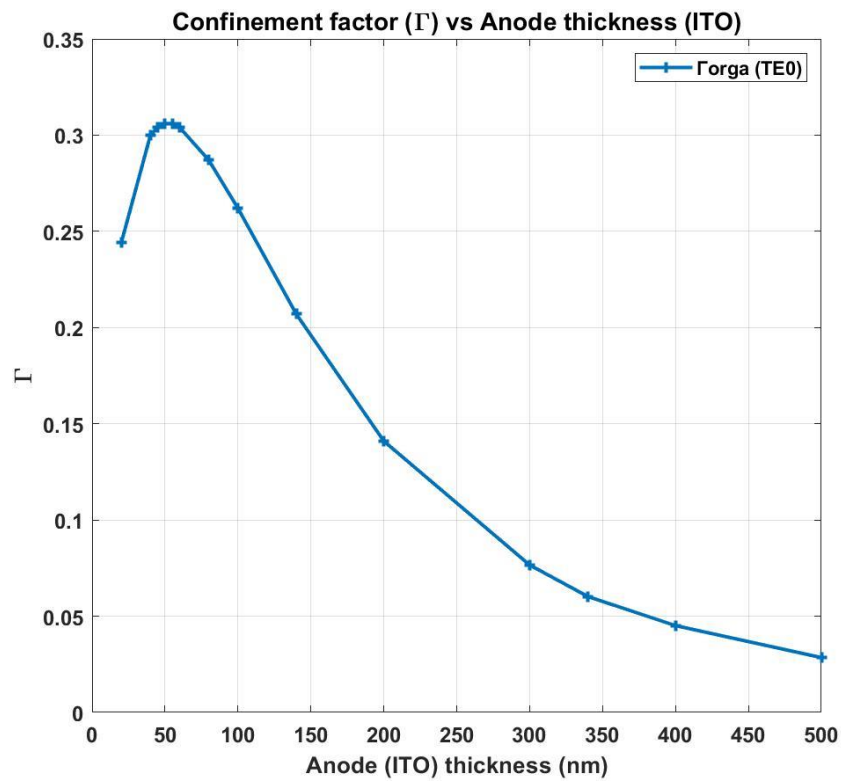
Figure 2. Confinement factor as function of the ITO thickness.
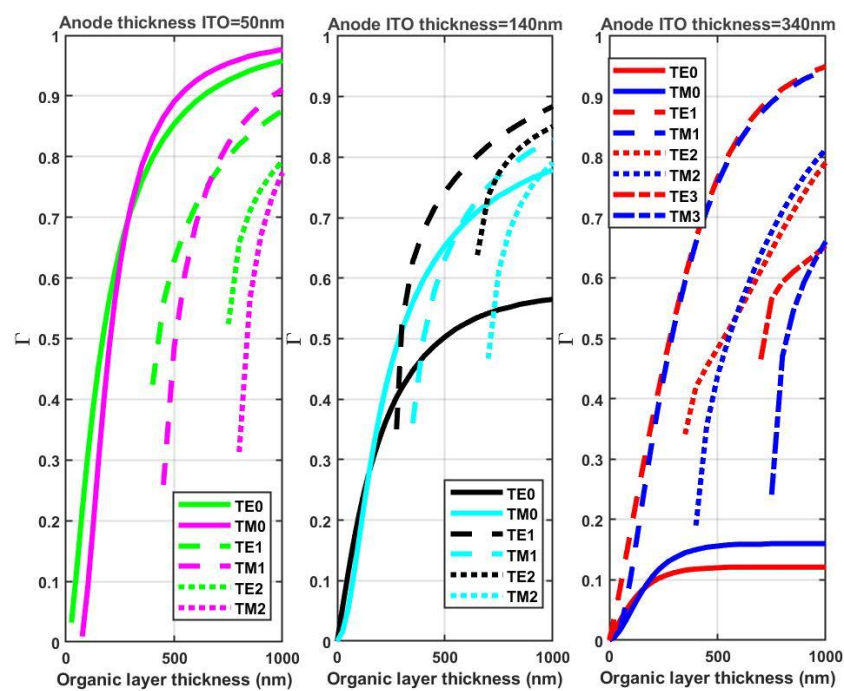
Figure 3. Confinement factor in organic layer vs organic thickness for ITO thickness for different TE and TM modes; 340 nm (red (TE) and blue ™), 140 nm (black (TE) and c™(TM)), and 50 nm (green (TE) and magenta (TM)).

The comparison between the three cases in Figure 3 shows a trend where the confinement factor curves decrease with respect to each other when the ITO layer thickness increases. More precisely, the TE_0 and TM_0 curves are located above the TE_1 and TM_1 curves. The latter are above the TE_2 and TM_2 curves. Lasing conditions are therefore more favorable for the TE_0 and TM_0. The trend still stands at a constant organic layer thickness, because the increase in the ITO thickness leads to a decrease in the confinement factor and eventually to an increase in the modes number (TE and TM). On the other hand, the increase in the thickness of the organic layers enhances the confinement factor.

Next, we would like to study more realistic organic layer thicknesses, knowing that a typical OLED thickness is $t_2 = 100$ nm, and that the half-wavelength thickness at $\lambda = 600$ nm and $n = 1.7$ is 125 nm [17]. Note that an organic heterostructure filling a half-wavelength micro-cavity is thicker than a standard OLED, which is expected to strongly reduce the current density due to the low carrier mobility of the organic films [18]. However, a 125 nm thick undoped OLED was reported by Coens with a current density above 1000 mA/cm^2 in DC regime [17]. This is an indication that despite a slightly larger OLED thickness, electrical performance will not suffer. The thickness of 200 nm has been reported by Adachi's group, with a doped (PIN) heterostructure type with enhanced mobility, thus offering better electrical performance than undoped OLEDs [14].

Table 2 presents the confinement factor for different cases with three different ITO thicknesses ($t_1 = 50$ nm, 140 nm and 340 nm) and three organic thicknesses ($t_3 = 200$ nm, 125 nm and 100 nm), as presented previously.

Table 2. Summary of the values for the different cases.

ITO Thickness t_1 (nm)	Organic Thickness t_3 (nm)	Γ			
		TE_0	TM_0	TE_1	TM_1
50	200	0.565	0.487	-	-
	125	0.385	0.19	-	-
	100	0.306	0.088	-	-
140	200	0.339	0.38	-	-
	125	0.247	0.226	-	-
	100	0.207	0.166	-	-
340	200	0.097	0.106	0.367	0.334
	125	0.073	0.065	0.231	0.163
	100	0.061	0.049	0.183	0.107

In the 50 nm case, with a thickness of $t_3 = 200$ nm, the Γ values of the TE_0 and TM_0 modes are as large as 0.56 and 0.49. For $t_3 = 125$ nm, the Γ values of the TE_0 and TM_0 modes are as large as 0.39 and 0.19. With a thickness of organic layer $t_3 = 100$ nm, the Γ value of TE_0 is as large as 0.31, while that of TM_0 is only 0.08. For these cases, the only existing modes are TE_0 and TM_0. Moreover, the TE_0 confinement factor is much larger than that of the TM_0, favoring the TE_0 for lasing.

In the $t_1 = 140$ nm case, the Γ values of the TE_0 and TM_0 modes are 0.34, 0.25, 0.21 and 0.38, 0.22, 0.17 for $t_3 = 200$ nm, $t_3 = 125$ nm and $t_3 = 100$ nm, respectively.

In the $t_1 = 340$ nm case, with an organic layer thickness of $t_3 = 200$ nm, the Γ values of the TE_0 and TM_0 modes are 0.09 and 0.10. Here, the TE_1 and TM_1 coexist with values of 0.37 and 0.33, respectively, for $t_3 = 200$ nm. In such a situation, it is very likely that TE_1 and TM_1 will reach the condition for lasing before TE_0 and TM_0 do. With a thickness of $t_3 = 125$ nm, the Γ of TE_0 and TM_0 are 0.07 and 0.06, respectively, while those of TE_1 and TM_1 are 0.23 and 0.16, respectively. For $t_3 = 100$ nm organic layer thickness, the Γ values of TE_0 and TM_0 are 0.06 and 0.04, respectively, while those of TE_1 and TM_1 are 0.18 and 0.11, respectively.

As a preliminary conclusion, for the three cases of ITO thicknesses, the highest confinement factor Γ is obtained with organic layer thickness $t_3 = 200$ nm. The optimum confinement factor $\Gamma = 0.56$ is obtained for the combination ($t_1 = 50$ nm and $t_3 = 200$ nm). As an undoped 200 nm thick organic hetero-structure may suffer from electrical performances far from the state of the art, a second optimum to be considered is with the combination ($t_1 = 50$ nm, $t_2 = 125$ nm): $\Gamma = 0.38$. In this case, the confinement factor difference between the TE$_0$ and the TM$_0$ modes is expected to favor the TE$_0$ more clearly than with the first optimum.

2.1.2. Effective Index Contrasts

The effective index contrast Δ_{neff} is the difference between the high effective index n_H, corresponding to the stack shown in Figure 1c, and the low effective index n_L for the stack, presented in Figure 1b $\left(\Delta_{neff} = n_H - n_L\right)$.

In general, the effective index n_{eff} is defined as the propagation constant β in the waveguide divided by the free space propagation constant k:

$$n_{eff} = \frac{\beta}{\kappa} \qquad (2)$$

where $\kappa = \frac{2\pi}{\lambda}$ is the vacuum wavenumber associated with the specified vacuum wavelength λ. n_{eff} is not just a material property but depends on the geometry of the waveguide, e.g., the thickness of the waveguide. The effective index contrast is one of the key parameters that defines the quality factor of the laser cavity. Indeed, a lower effective index contrast causes a lower mirror reflectivity and thus a smaller quality factor; consequently, it decreases the amplification rate, thereby enhancing the laser threshold. The goal of this study is to identify the optimum waveguide geometry which offers the highest effective index contrast Δ_{neff}. It is evaluated as a function of the SiO$_2$ layer thickness t_2 for the nine combinations of t_1 and t_3.

Figure 4 presents the effective index contrast Δ_{neff} as a function of the SiO$_2$ layer thickness t_2 plotted with a logarithmic scale for three ITO layer thicknesses, $t_1 = 50$ nm (green), 140 nm (blue), and 340 nm (red), and for three organic layer thicknesses, $t_3 = 100$ nm (solid line), 125 nm (dashed line), and 200 nm (dotted line). The trends seen in the different curves is an increase in the effective index contrast Δ_{neff} from zero to higher values up to 0.07, when t_2 is increased and t_1 is decreased.

For the $t_1 = 50$ nm case, the highest index contrast $\Delta_{neff} = 0.071$ is obtained with $t_3 = 200$ nm. For $t_2 = 300$ nm, $t_2 = 100$ nm, and $t_2 = 50$ nm (these are achievable SiO$_2$ thicknesses to be obtained with an HSQ photoresist), the index contrasts are $\Delta_{neff} = 0.061$, $\Delta_{neff} = 0.035$, and $\Delta_{neff} = 0.021$, respectively. For the $t_1 = 140$ nm case, the highest index contrast $\Delta_{neff} = 0.057$ is obtained with $t_3 = 200$ nm and $t_2 = 300$ nm. For $t_2 = 100$ nm and $t_2 = 50$ nm, the index contrasts are larger than for the $t_1 = 50$ nm case and given by $\Delta_{neff} = 0.042$, and $\Delta_{neff} = 0.027$, respectively. For the $t_1 = 340$ nm case, the highest index contrast $\Delta_{neff} = 0.016$ is obtained with $t_3 = 200$ nm and, $t_2 = 300$ nm.

Table 3 summarizes the values of effective index contrast Δ_{neff} for nine different combinations given by:

- Three ITO layer thicknesses t_1: 340 nm, 140 nm, and 50 nm.
- Three organic layer thicknesses t_3: 100 nm, 125 nm, and 200 nm.
- Three SiO$_2$ layer thicknesses t_2 (300 nm, 100 nm, and 50 nm). This choice is based on the capacity of the fabrication.
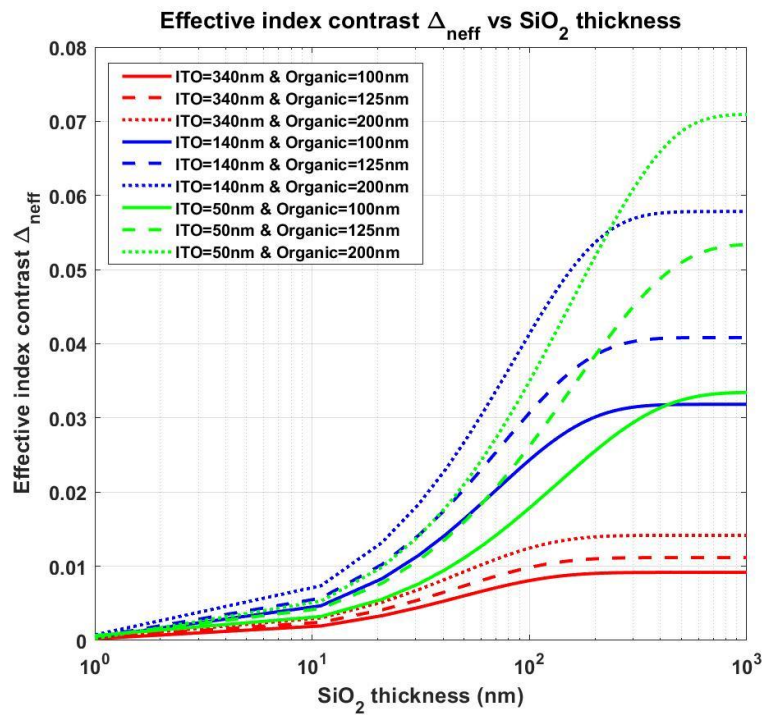
Figure 4. Effective index contrast vs. SiO$_2$ layer thickness for ITO thickness; 340 nm (Red), 140 nm (blue) and 50 nm (green) and organic thickness; 100 nm (continued line), 125 nm (discontinued line), and 200 nm (point line).

Table 3. Effective index contrast.

ITO Thickness t_1 (nm)	Organic Thickness t_3 (nm)	Δ_{neff} SiO$_2$ Thickness t_2 (nm)		
		50	**100**	**300**
50	100	0.0107	0.017	0.029
	125	0.016	0.026	0.045
	200	0.021	0.035	0.061
140	100	0.016	0.024	0.031
	125	0.021	0.031	0.040
	200	0.027	0.041	0.057
340	100	0.006	0.008	0.009
	125	0.007	0.009	0.011
	200	0.009	0.012	0.014

The highest effective index contrast $\Delta_{neff} = 0.061$ is obtained with $t_1 = 50$ nm, $t_2 = 300$ nm, and $t_3 = 200$ nm, which we will consider to be the optimum case in what follows.

As a conclusion, we highlight three design rules: firstly, higher effective index contrasts are achieved with thinner ITO thickness t_1. Among the available options, the 340 nm case should be disregarded due to its low effective index contrast, while the 50 nm thickness is preferable because it provides one of the highest effective index contrasts. Secondly, as the thickness of the SiO$_2$ layer (t_2) increases, the effective index contrast also increases.

In Table 3, the "50 nm" column exhibits the lowest effective index contrast, and thus the corresponding cases can be disregarded. Finally, an increase in the thickness of the organic layer (t_3) results in a higher index contrast. However, the optimal thickness of the organic layer will depend on the emission wavelength. As stated previously, the most

efficient emission is obtained with a half-wavelength optically thick OLED stack. Moreover, the emitting layer is to be located at the anti-nodes of a transversal standing wave in order to maximize the coupling of organic emitting dipoles with the optical field so as to increase the light emission [19]. In the case where a standard $t_1 = 140$ nm ITO is used with a standard $t_3 = 100$ nm organic stack and with $t_2 = 300$nm, the index contrast is 0.031 and the low effective index is $n_L = 1.638$. At $\lambda = 625$ nm, the quarter wavelength is 156 nm, and the geometrical thickness of 95 nm is not far from t_3.

2.2. Micro-Cavity: Reflectance Study

We aim to identify the optimal geometry maximizing the quality factor.

The Matrix transfer method is used to calculate the reflectance, considering the DFB cavity is a periodic stack (grating) with an alternation of high index n_H and low index n_L materials. Each layer of the stack is considered infinitely extended in the x and y directions while the incident light propagates in the z direction, as indicated in Figure 5.
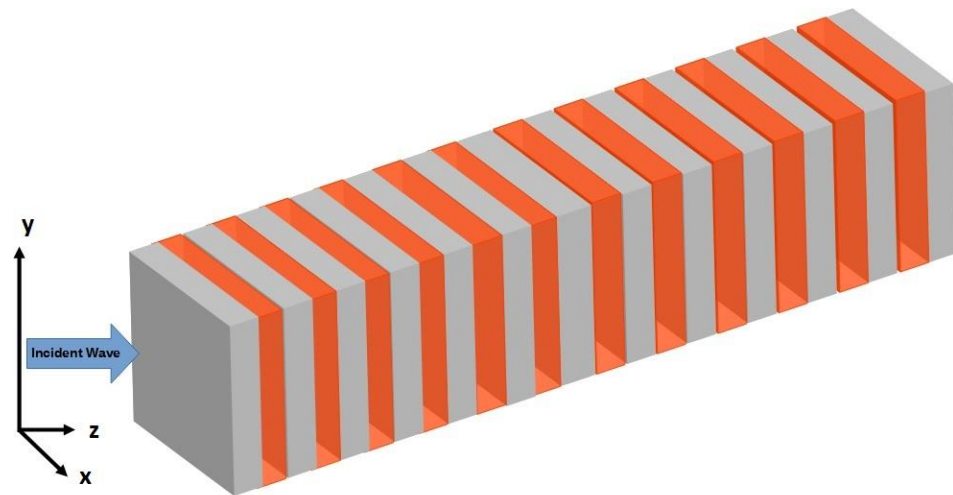

Figure 5. Light propagation in a DFB cavity.

The targeted DFB laser cavity apriori consists of a left mirror (Mirror 1) and a right mirror (Mirror 2) surrounding a defect zone. In conventional lasers, the gain medium is located in between the mirrors (defect zone), whereas in our case, the gain medium is distributed along the structure as part of the high-index layers (orange in Figure 5).

The study is split into two parts: as the first step, we consider a single mirror and investigate how the reflectance evolves with the number N of pairs and for different cases of effective index contrasts. In the second step, we introduce defects in between mirrors. Then we attempt to maximize the quality factor.

2.2.1. Single DFB Mirror

In this first step, we consider a single mirror made of N pairs of quarter wavelength $(\lambda/4)$ layers of high index (n_H) and low index (n_L), with the central wavelength $\lambda_c = 605$ nm corresponding to the peak wavelength of the DCM. (Similar reasoning would apply to other wavelengths and materials.) Each mirror starts and ends with high index layers and thus is made of N pairs and a single high-index layer, as shown in Figure 6. We neglect the absorption; thus, each layer is characterized by a purely real index. In the absence of absorption, the reflectance R and the transmittance T are linked by the trivial relationship $R + T = 1$, as shown in Figure 7. T and R have been calculated with $N = 100$ pairs (plus a high-index layer) for the higher index contrasts listed in Table 3, to which we added $\Delta_{neff} = 0.25$, corresponding to the index difference between the bulk organic material $n = 1.7$ and that of the SiO$_2$, with $n = 1.45$.
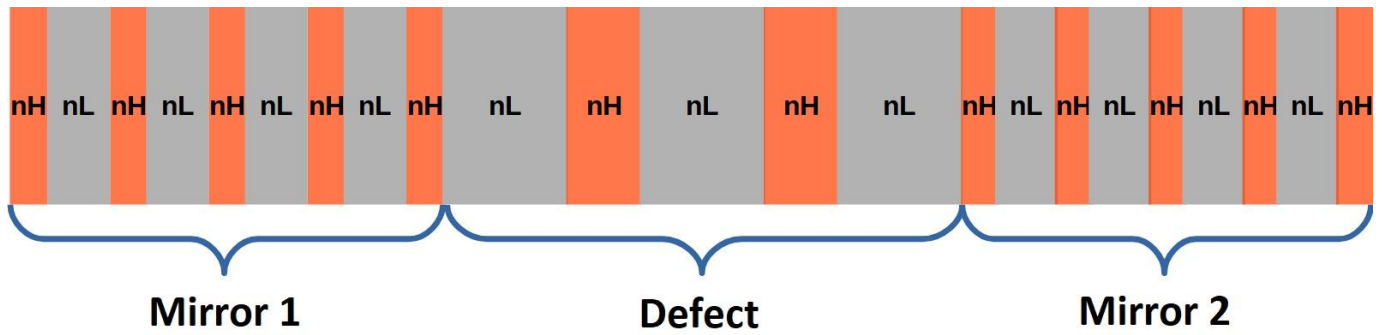
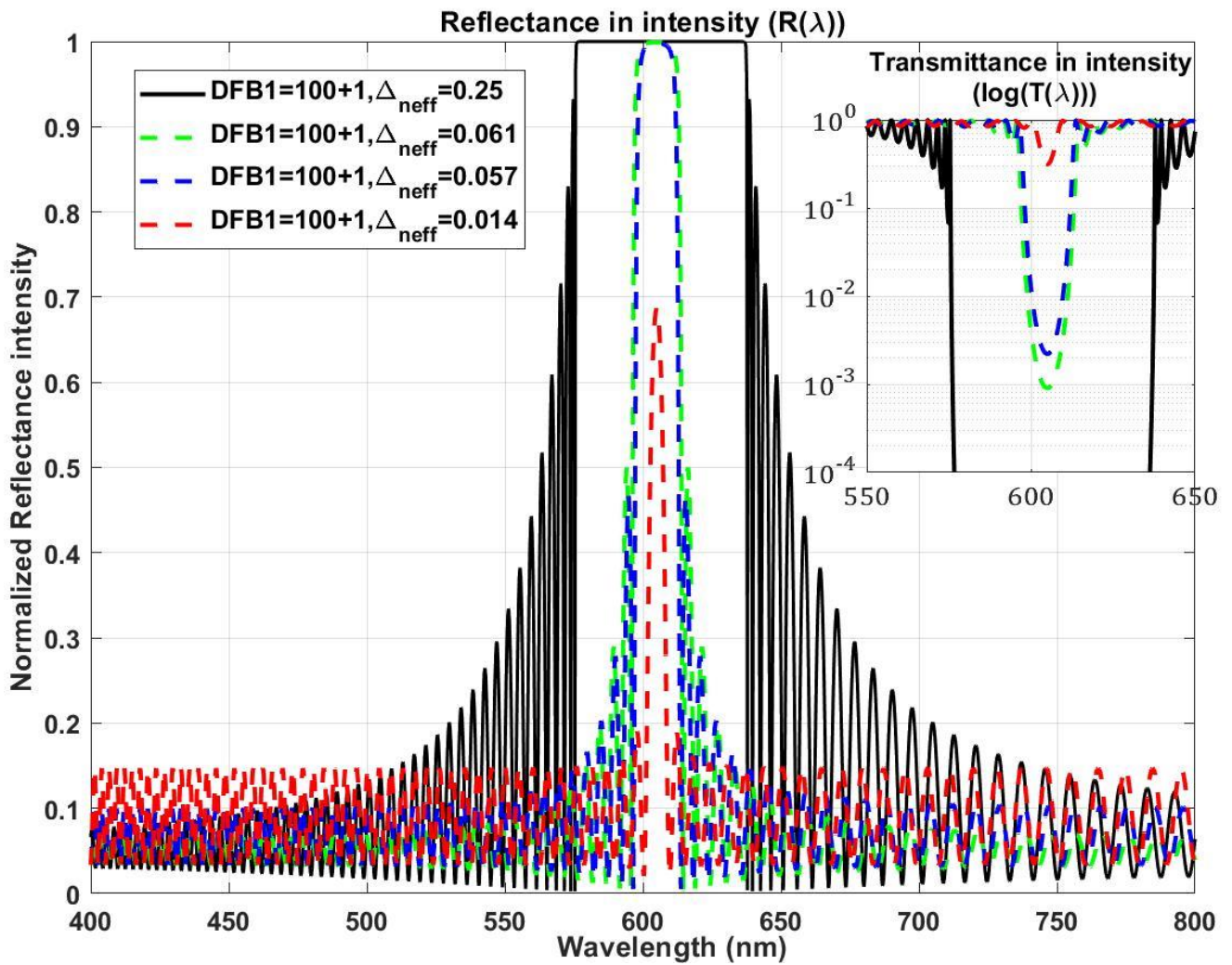**Figure 6.** Detailed structure of a DFB cavity with mirrors and defects.

Figure 7. Reflectance and transmittance (inset) calculated for $N = 100$ pairs (+1 high index layer) and for the different index contrasts listed in Table 3: (black) offers the largest forbidden bandgap. R and T calculated for $t1 = 50$ nm and $t2 = 300$ nm (green), R and T calculated for $t1 = 140$ nm and $t2 = 300$ nm (blue). R and T calculated for $t1 = 340$ nm and $t2 = 300$ nm (red). These for $t3 = 200$ nm.

The various reflectances presented in Figure 7 exhibit band-pass properties with the largest values of the reflection in wavelength ranges $\Delta\lambda$ centered on $\lambda_c = 605$ nm. Transmittances (inset in Figure 7) exhibit notch-filter properties with the same bandwidth $\Delta\lambda$. In some cases, the bandwidth $\Delta\lambda$ is the one-dimensional equivalent of the forbidden bandgap of photonic crystals.

In Figure 7, the width $\Delta\lambda$ of the forbidden bandgaps can be compared for the different index contrasts:

- $R_1(\lambda)$ is the reflectance of the DFB mirror calculated with the large-index contrast $\Delta_{neff} = 0.25$ (black solid line). The reflectance is close to unity from 589 nm to 654 nm, resulting in a full-width at half-maximum (FWHM) bandwidth of $\Delta\lambda_1 = 65$ nm.
- $R_2(\lambda)$ is the reflectance calculated with the index contrast $\Delta_{neff} = 0.061$, corresponding to the optimum value listed in Table 3 ($t_1 = 50$ nm, $t_2 = 300$ nm and $t_3 = 200$ nm) plotted in green. The calculated FWHM bandwidth is $\Delta\lambda_2 = 18$ nm.
- For the index contrast $\Delta_{neff} = 0.057$ (blue), the FWHM bandwidth is $\Delta\lambda_3 = 15$ nm.
- For the index contrast $\Delta_{neff} = 0.014$, T and R are plotted in red in Figure 7. For this value, and in the case where $N = 100$, the FWHM bandwidths of the reflectance can be calculated but the corresponding peak values hardly exceed 0.6, which indicates that no forbidden bandgap exists.

A trend can be identified: the width of the transmittance becomes narrower when the index contrast is reduced. This is similar to what is observed with two-dimensional photonic crystals, with the forbidden bandgap depending on the index contrast.

Note that the forbidden bandgap $\Delta\lambda_2 = 18$ nm, corresponding to the maximum calculated in Table 3, is about 4 times narrower than the FWHM of the electroluminescence spectra of the dopant, which is about 80 nm [20]. The laser cavity will therefore be efficient only in a small spectral range of the laser gain spectrum, and spontaneous and stimulated emission will very likely occur simultaneously.

We investigate the effect of the number of pairs N on the width $\Delta\lambda$ of the reflectance windows from which we will estimate the forbidden bandgap. The number of pairs is varied from $N = 2$ (+1 layer) to 210 pairs (+1 layer), and for each number N of pairs the reflectance is calculated for $\Delta_{neff} = 0.25$ and for the four different index-contrast values listed in the last column of Table 3. The width in wavelength of the windows for which the reflectance is at its maximum can be estimated at half maximum, giving a range $\Delta\lambda$ from which the forbidden bandgap can be estimated. The result is plotted in Figure 8. The different width $\Delta\lambda$ of the reflectance windows calculated as a function of N for the four better index contrasts of each thickness of ITO are presented in the left axis (orange lines), while the maximum of the reflectance windows corresponds the right axis at the top of Figure 8 top (blue lines). The amplitudes of the reflectance calculated for $\Delta_{neff} = 0.061$, $\Delta_{neff} = 0.057$, and $\Delta_{neff} = 0.25$ exceed 0.95 for $N \geq 100$, whereas for the lower-index contrast $\Delta_{neff} = 0.014$ the amplitudes of the reflectance do not exceed 0.95 even for pair numbers N as large as 200. At the bottom of Figure 8, the width $\Delta\lambda$ is plotted for the cases $R \geq 0.95$ as an estimation of the forbidden bandgap. It shows a small decrease in the width $\Delta\lambda$ of the forbidden bandgap with the number N of pairs. With the "bulk" index contrast $\Delta_{neff} = 0.25$, the forbidden bandgap converges to $\Delta\lambda_1 = 65$ nm when $N > 100$. For $\Delta_{neff} = 0.061$, the forbidden bandgap is 18 nm and 16 nm for $N = 80$ and 200 pairs, respectively.
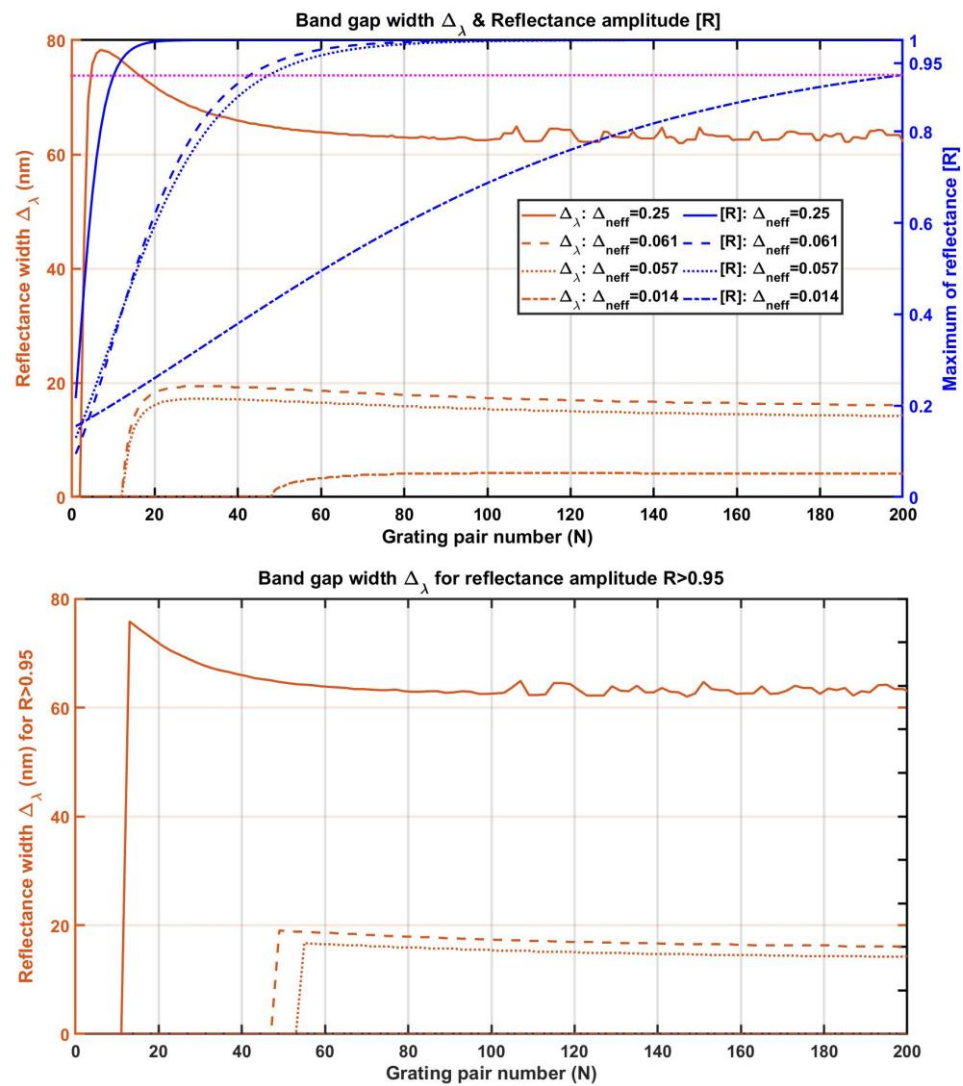
Figure 8. Width FWHM of the reflectance windows as a function of the number *N* of pairs of layers. (**top**) Width of the reflectance windows calculated for four index contrasts (left axis) and the peak wavelength of the reflectance windows for the same index contrasts (right axis). (**bottom**) Values of the FWHM of the reflectance windows as a function of the number *N* of pairs for peak reflectance above 0.95.

2.2.2. Cavities Consisting of DFB Mirrors and Defects in between

As a second step, we investigate DFB cavities designed with the following rules:

- Cavities are made of a left and a right mirror with a defect in between them.
- Mirrors are made of *N* pairs of quarter-wavelength $(\lambda/4)$ layers alternating between high-index (n_H) and low-index (n_L), where λ is the central wavelength under consideration. Each mirror starts and ends with high-index layers (n_H), and thus is made of $2N + 1$ layers. This is particularly important when the number *N* of pairs is small (<10).
- The defect is made of high index (n_H) and low index (n_L), with a total optical thickness that is an odd number of half wavelengths such that after one round-trip the accumulated phase is a multiple of the wavelength, resulting in constructive interference. Because each mirror starts and ends with high-index layers, the defect must start and end with a low-index layer (n_L). It is composed of *M* pairs of alternating half-wavelength thick high-index (n_H) and low-index (n_L) layers. The total optical thickness equals $2M + 1$. This constitutes a second-order grating "DFB2". As mentioned before, the role of the second-order grating is to provide a partial outcoupling

of light in the direction perpendicular to the plane of the grating at the resonance wavelength. This offers the possibility to measure the light intensity of the device more easily.

The resonances are centered at the central wavelength $\lambda_c = 605$ nm, with $\Delta\lambda$ the full-width at half-maximum (FWHM). This is an indication that they are suitable as laser cavities centered on the maximum DCM electroluminescence.

Note that with the above-described defect, the FWHM reflectance window (forbidden bandgap) is enlarged (see the dotted black curve in Figure 9). For example, with $N = 50$ pairs and $M = 5$ for the second-order grating defect, $\Delta\lambda = 90$ nm, which represents an increase of 50% compared to the reference spectrum extracted from Figure 7. The reference spectrum is plotted again with a black solid line in Figure 9. This enhancement of the FWHM of the forbidden bandgap is advantageous for a reduction of the spontaneous emission components of the spectra with respect to that of the stimulated emission, potentially allowing for a less noisy detection of the stimulated emission components.
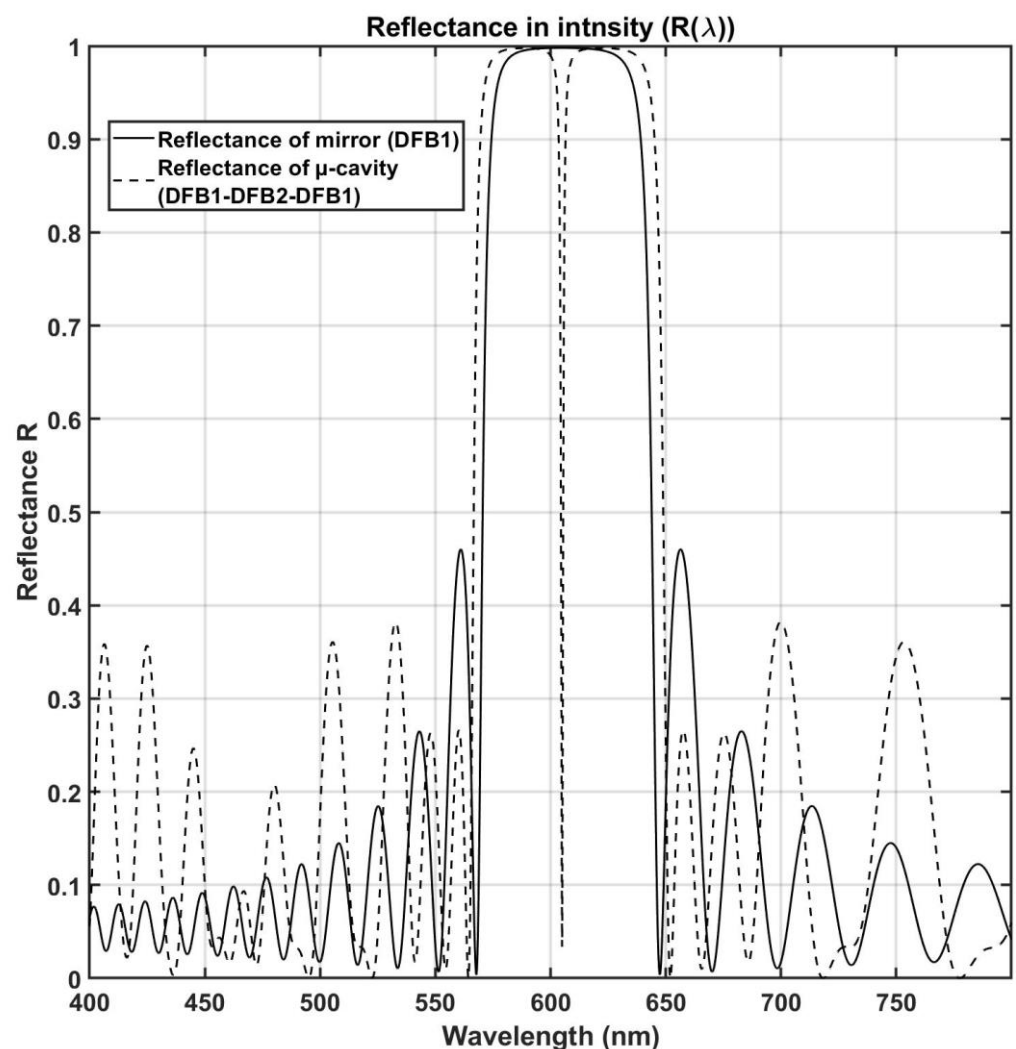

Figure 9. Reflectance of a single mirror (DFB1) (black solid line) and two mirrors (DFB1) surrounding defects (DFB2) (thin black-dashed line).

2.2.3. Quality Factor of DFB Cavities

The quality factor of the passive (empty) cavity can be calculated from $\delta\lambda$ the full-width at half-maximum (FWHM) of the resonance:

$$Q = \frac{\lambda_c}{\delta\lambda} \tag{3}$$

For example, with the left and right mirrors made of $N = 50$ pairs plus one n_H layer, and a second-order grating with $M = 5$ exhibits a FWHM resonance $\delta\lambda = 1.6$ nm, resulting in a quality factor of $Q = 387$ (see Figure 9).

To compare the different configurations and identify the most relevant one, we compare the quality factors Q of the different index contrasts in Figure 10. Using the matrix transfer method, we compute the transmittance while varying the pair number N between 1 and 200, with the pairs of the defect is fixed to $M = 2$ (5 layers), and we calculate the FWHM resonance linewidth. The quality factor is plotted with a logarithmic scale as a function of the pairs N in each mirror.
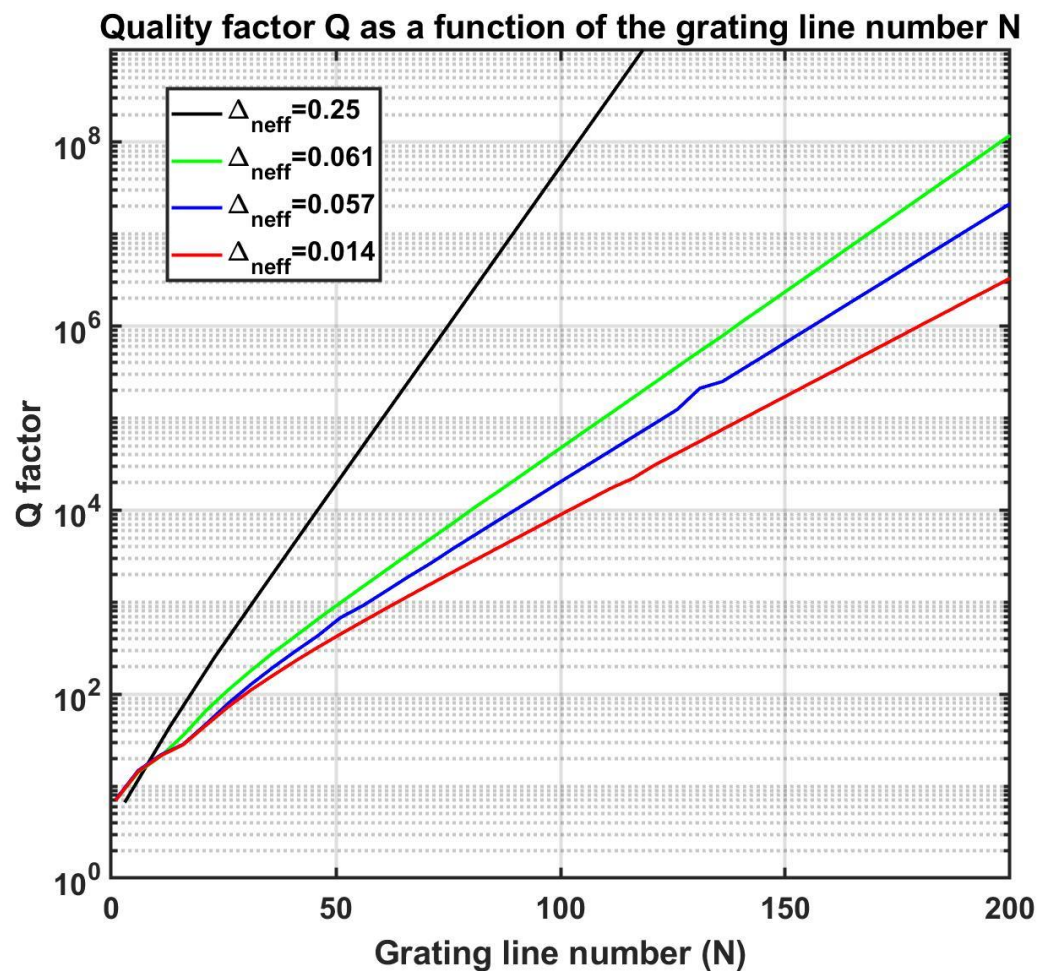

Figure 10. Quality factors of the different types of cavities with different types of defects a function of the number of grating lines in the mirrors.

First of all, it is to be noted that the quality factors increase with N. The slope in the logarithmic scale appears linear, meaning an exponential increase in Q. This slope is different for the different index contrasts ($\Delta_{neff} = 0.25$, black, $\Delta_{neff} = 0.061$, green, $\Delta_{neff} = 0.057$, blue, $\Delta_{neff} = 0.014$, red). The better the index contrast, the larger the slope of the quality factor is.

With these simulations performed without absorption, the quality factors in excess of 1000 are obtained with $N > 51$ ($N > 65$, and $N > 87$, respectively) for $\Delta_{neff} = 0.061$, green ($\Delta_{neff} = 0.057$, blue and $\Delta_{neff} = 0.014$, red, respectively). For $\Delta_{neff} = 0.061$ (green), quality factors $Q \geq 3000$ and $Q \geq 5000$ are obtained with $N \geq 66$ and $N \geq 72$. For $\Delta_{neff} = 0.057$ (blue), quality factors $Q \geq 3000$ and $Q \geq 5000$ are obtained with $N \geq 73$ and $N \geq 81$. Quality factors $Q > 1,000,000$ can be obtained with $N > 141$ and $N > 157$, respectively, for $\Delta_{neff} = 0.061$ (green) and $\Delta_{neff} = 0.057$ (blue). The quality factor barely exceeds $Q = 1000$ for $N = 200$ in the less favorable case, with $\Delta_{neff} = 0.014$.

The optimum geometrical and optical parameters of the micro-cavity are summarized in Table 4.

Table 4. Optimum geometrical and optical parameters of the device.

	Best Optimum	**Optimum**
ITO thickness t_1 (nm)	50	140
Organic thickness t_3 (nm)	200	200
SiO$_2$ thickness t_2 (nm)	300	300
l_{1L} (nm)	98	92
l_{1H} (nm)	102	95
N	200 pairs + 1	200 pairs + 1
M	10 pairs + 1	10 pairs + 1

These results were obtained without taking into account the absorption of ITO and of SiO$_2$. Moreover, the absorption of the organic semiconductors is not taken into account in the calculation of the reflectance. This leads to an overestimation of the quality factor compared to the reality. In order to achieve the same quality factor as the real case, it is necessary to take a larger number of periods, *N*, than calculated. Note that the transfer matrix method does not take into account the diffraction perpendicular to the plane of the grating and as such also overestimates the quality factor.

3. Fabrication

The fabrication of the cavity is based on e-beam lithography. To pattern the micro-cavity, we use the HSQ as a negative electro-sensitive resist. A 300 nm thick layer of this resist is coated on a glass sample, which is already coated with 140 nm or 340 nm of the ITO layer. After the insulation with the SEM (Raith Pioneer), a development step is necessary to reveal the structure of the micro-cavity.

Samples

On a glass sample coated with 140 nm of ITO, 30 patterns have been e-beam lithographed in a 300 nm thick HSQ electron-sensitive resist. The 30 motifs are divided into 5 rows and 6 columns corresponding to 5 different geometries and 6 different doses, as shown in Figure 11. Each pattern, repeated every 500 μm horizontally and 400 μm vertically, consists of three sections: the first and third sections are made of parallel lines with width l_{1l}, varying between 107 and 121 nm, and spaced by l_{1H}, varying between 91 nm and 103 nm; the second section is made of 10 parallel lines with a nominal width of $l_{2l} = 2\,l_{1l}$ and 11 spacings with a nominal width of $l_{2H} = 2\,l_{1H}$. The length of Section 2 of the cavity varies between 3.5 and 5.6 μm.
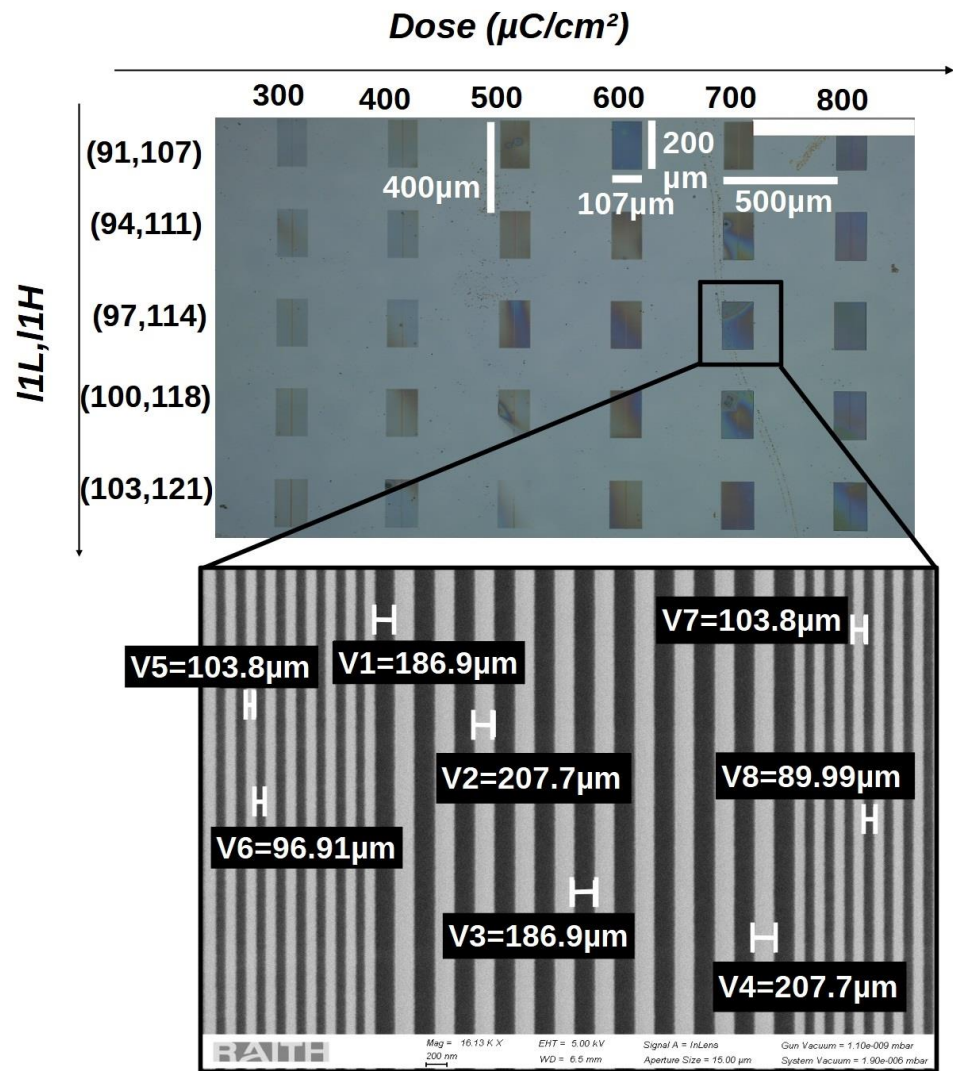
Figure 11. Sample: matrix of micro-cavity with different doses observed by optical microscope (**top**), example of micro-cavity observed by SEM (**bottom**).

Five couples (l_{1H}, l_{1l}), defining five different geometries, are used, as indicated in Table 5. The nominal resonance wavelength of the quarter-wavelength grating reads

$$\lambda Bragg = 2(n_H l_{1H} + n_L l_{1H}) \tag{4}$$

with much uncertainty about the effective indices n_H and n_L. Because of this uncertainty, the bulk refractive indices are used in a first approach. The nominal resonance wavelengths are given in the first column of Table 5.

From l_H and l_L, the dimension of the spacing and the line widths, the nominal Bragg wavelength is calculated according to (4) and using the bulk refractive indices $n_H = 1.7$ and $n_L = 1.45$, resulting in 622 nm $\leq \lambda_{Bragg} \leq$ 682 nm.

Six different doses are introduced to investigate the potential impact on the geometry and thus on the effective resonance wavelength. This is an indirect way of varying l_H with respect to l_L, because when the dose is increased, the width of the HSQ lines increases at the cost of the decrease in the spacing. This is due to electron diffusion.

The laser gain medium evaporated on the patterns consists of 200 nm of Alq3 doped with 2% DCM2. For this concentration, the maximum spontaneous emission is obtained at 607 nm.

Table 5. Nominal dimensions of micro-cavity lines and spacing.

Nominal Bragg Wavelength λ_{Bragg} (nm)	l_{1H} (nm)	l_{1l} (nm)	l_{2H} (nm)	l_{2l} (nm)	Length of Section 2 of the Cavity (μm)
622	91	107	183	214	4.085
642	94	111	189	221	4.150
662	97	114	195	228	4.300
682	100	118	201	235	4.421
702	103	121	206	242	4.523

4. Validation: Laser Properties of DFB Patterns under Optical Pumping

This section is devoted to the characterization and analysis of micro-cavities filled with an organic laser gain medium under optical pumping. To check that the DFB patterns offer the expected properties of a laser cavity, the samples prepared according to the fabrication process are submitted to optical pumping. Among the properties expected from patterns that constitute laser micro-cavities, the two most important are the following: Firstly, the matching of the micro-cavity resonance with the maximum of the organic material photoluminescence, and, secondly, a high-quality factor ideally above $Q \simeq 1000$ to achieve threshold current densities in the kA/cm^2 range.

4.1. Experimental Setup

We pump the emitting layer, deposited on the DFB grating, with a tripled Nd-Yag laser ($\lambda = 355$ nm) with a pulse duration of 12 ns via a ×40 microscope objective, resulting in a spot size estimated at 100 μm in diameter. The spot of detection is 10 μm in diameter, spatially separated from the pumping spot and tangent to that. The collected light is sent to a spectrometer (Ocean Optics 2000+ with 0.2 nm resolution and analyzed in the wavelength range [344.79 nm–1036.61 nm]). Another spectrometer (Ocean Insight Flame) offers a resolution of 0.05 nm with a wavelength range of 578.91 nm to 688.66 nm. The energy of the pump is varied with a half-wavelength plate followed by a linear polarizer, and the spectrum is acquired by integrating for over 10 s. The maximum of the spectrum is used to quantify the output light.

4.2. Experimental Results

Figure 12 shows the output light intensities for different energy densities of the pump in log–log scale. The curve exhibits an "S" shape typical of laser behaviors. In A (blue dot) and B (red dot), the spectra shown in blue and red in the inset (b) exhibit a FWHM line width ($\delta\lambda$) of 61 nm and 57 nm, respectively. In C (green dot), with a pump energy of 125 μJ/cm^2, the spectrum shows a peak enhancement with a linewidth reduction to 47 nm. Above this pump energy value, the light output increases more rapidly, indicating that the threshold value for lasing was exceeded. In D (cyan dot) for 167 μJ/cm^2, E (magenta dot) for 269 μJ/cm^2, and F (orange dot) for 477 μJ/cm^2, the spectra measured with the 0.2 nm resolution spectrometer shown in the inset (c) narrow further down to 1.1 nm, 1.3 nm, and 1.7 nm, respectively. With the 0.05 nm resolution spectrometer, not only the FWHM are measured respectively down to 0.38 nm, 0.46 nm, and 0.73 nm, but several peaks also appear, indicating a multimode emission, as displayed in Figure 12 (inset (d)). The small increase in the linewidth above the threshold is thus explained by the multimode emission, as in Fabry-Perot lasers and contrary to DFB lasers.
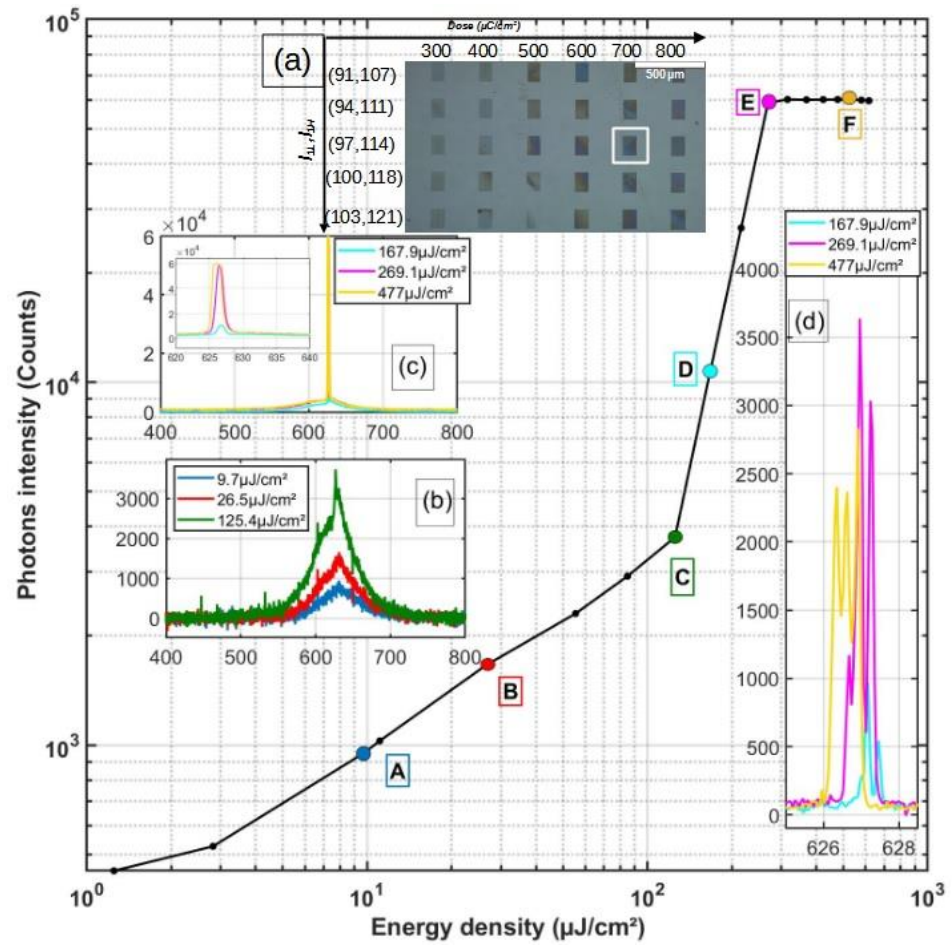
Figure 12. S curve behavior of micro-cavity: (**a**) the sample, (**b**) spectrum in A (blue line), in B (red line) and in C (green line), (**c**) spectrum in D, E and F points (cyan, magenta, and orange lines, respectively), (**d**) zoom of the inset (**c**).

The origin of these multiple modes can be found either in the different TE and TM modes allowed by the 140 nm thick ITO planar waveguide and/or in the multiple reflections from adjacent cavities. The free spectral range (FSR) of $\Delta\lambda \simeq 0.25 \pm 0.05$ nm gives a first indication about this origin. The cavity length corresponding to this FSR is $e = \lambda_0^2/(2n_a\Delta\lambda) \simeq 500$ μm, with $\lambda_0 = 627$ nm, the central wavelength, and $n_a = 1.6$, the average refractive index of the cavity medium. This indicates that the FSR probably corresponds to the spacing between two adjacent cavities as in the inset (a).

In the case of 140 nm thick ITO, 200 nm thick organic layers, and 300 nm of HSQ, the system provides only two modes (TE_0 and TM_0) as shown in Table 2, whereas five peaks are visible in the inset (d) of Figure 12. This indicates that the multimode emission does not find its origin in the waveguide modes.

The FWHM of the different peaks are estimated at 0.12 nm and 0.13 nm for the cyan spectra (167 μJ/cm^2), 0.17 nm and 0.14 nm for the magenta spectra (269 μJ/cm^2), and 0.17 nm for the yellow spectra (477 μJ/cm^2). Under lasing operation, the ratio $(\lambda/\delta\lambda)$ is different from the cold-cavity quality factor but still gives an estimation in the range of 3687 to 5226, as presented in Table 6.

Table 6. Ratios of the different peaks.

Pump Energy (μJ/cm²)	Resonance Wavelength λ_R (nm)	FWHM δ_λ (nm)	$Q_{warm} = \frac{\lambda_R}{\delta_\lambda}$
167 μJ/cm² (Cyan)	627.2	0.12	5226
	627.5	0.13	4826
269 μJ/cm² (Magenta)	627.0	0.17	3688
	627.2	0.14	4480
477 μJ/cm² (Yellow)	626.9	0.17	3687

It is expected that the observed resonance wavelength deviates from the nominal resonance wavelength because of three types of uncertainties:

- the effective indices that depend on the effective thickness of the different layers;
- the width of the grating lines that depends on the geometry design and the dose;
- the electroluminescence peak of the organic material that varies with the effective concentration of the dopant in the matrix [21]

To investigate the effects of the different parameters, we fabricated the matrix shown in Figure 11 with different geometries and different doses to quantify how the emission wavelengths change in the different cases. Figure 13 presents in different colors the different spectra for the different cavities (see the upper-right inset) framed with the same color, under an optical pump excitation of 211 μJ/cm². Only four cavity geometries allow for laser emission, as shown by the magenta (case 1), green (case 2), blue (case 3), and red (case 4) spectra. These correspond to patterns with nominal Bragg wavelengths of 662 nm ($l_L = 114$ nm, $l_H = 97$ nm) and 682 nm ($l_L = 118$ nm, $l_H = 100$ nm) and doses of 600 μC/cm², 700 μC/cm², and 800 μC/cm².
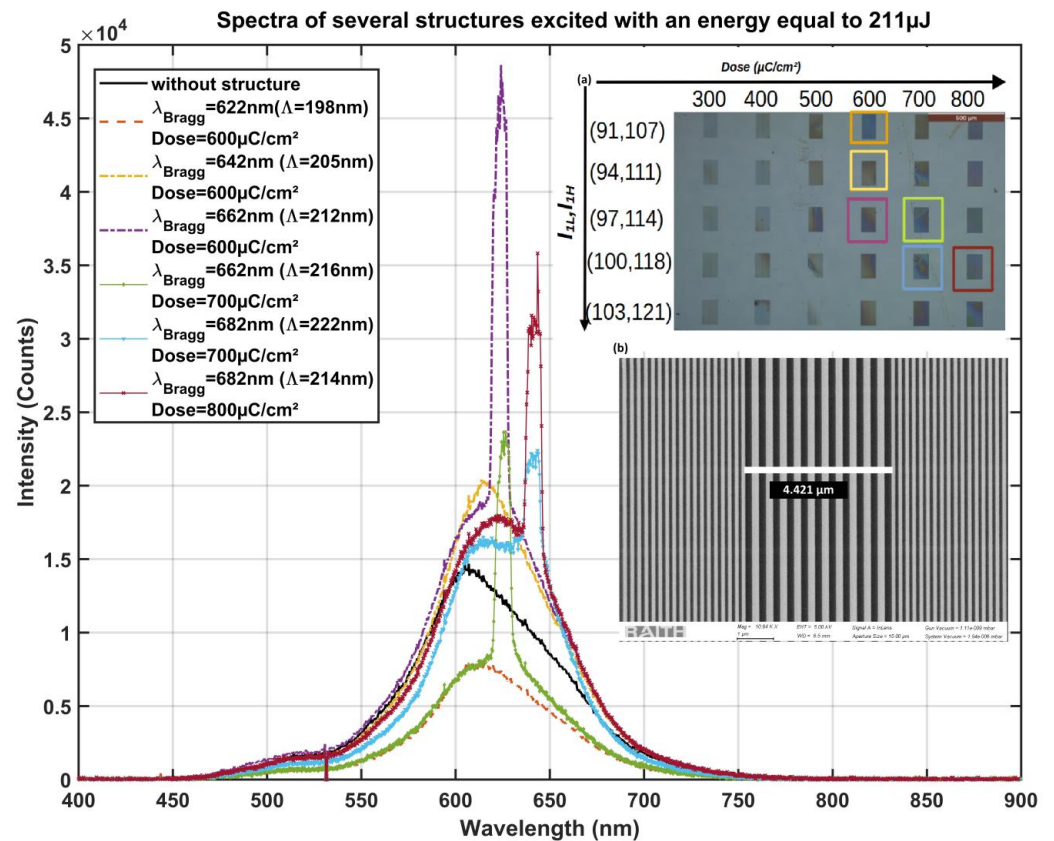

Figure 13. Spectra of the light coupled by the second order grating (**b**) of different structures framed in colors (**a**).

The observed laser wavelengths are 624.1 nm, 625.5 nm, and 643.5 nm, corresponding to the relative deviations of 5.7%, 5.4%, and 5.6% with respect to the nominal wavelengths (Table 7). The observed peak wavelength is systematically smaller than the nominal wavelength, indicating that the refractive index is likely overestimated. Note that from line to line, the relative uncertainties of the linewidth calculated from Table 7 (respectively, cases 1–4) are $\pm2\%$, 2.8%, 2.6%, and 3.7%, respectively, which are less than the relative deviations of the Bragg wavelength, confirming the overestimation of the index.

Table 7. Wavelength detuning between the nominal Bragg wavelength and emission.

Nominal Wavelength λ_{Bragg} (nm)	Dose (μC/cm²)	Width of SiO₂ Line l_L (nm)		Width of Spacing l_H (nm)		Observed Peak Wavelength λ_R (nm)
		l_{Lmin}	l_{Lmax}	l_{Hmin}	l_{Hmax}	
		Without cavity				607
622		103		90	97	615
642		105	109	92		613.6
662	600 (case 1)	115		93	101	624.1 (lasing)
	700 (case 2)	119		91	102	626.5 (lasing)
682	700 (case 3)	116	129	95	102	643.5 (lasing)
	800 (case 4)	138	160	60	90	643.5 (lasing)

5. Conclusions

In the context of an organic laser diode, we have presented a study on the design of a mixed-order DFB cavity, which was validated experimentally. The main challenge of this study was to have the resonance of the cavity attuned to the electroluminescence spectrum of the gain material to optimize the laser conditions.

The mixed-order DFB cavity considered consists of three sections: two first-order gratings separated by a grating of second order. The first-order gratings play the role of mirrors, confining the light within the structure, whereas the second-order grating enables the light to be emitted perpendicular to the cavity and detected. DFB mirrors are made of gratings with quarter-wavelength lines of low-effective index (n_L) lines alternated with high-effective index (n_H) spacing. The index n_H is the effective index of the OLED stack made of ITO covered with organic layers, whereas n_L is the effective index of the ITO/SiO₂/Organic stack.

The proposed design method has four steps. It takes into account the effective index in the calculation of the resonance by combining the optical waveguide analysis and the transfer-matrix formalism. The findings of this study provide valuable insights into the conception of cavities.

In the first step, conducted with the optical waveguide analysis, we identified the conditions of the ITO layer thickness to maximize the confinement factor Γ. We concluded that with an ITO layer as thin as $t_1 = 50$ nm (respectively 140 nm) and an organic layer as thick as $t_3 = 200$ nm, the confinement factor is at its maximum at $\Gamma = 0.565$ (respectively 0.339).

In the second step, conducted through optical-waveguide analysis, the index contrast is maximized by identifying the optimal SiO₂ and organic layer thicknesses that maximize the index contrast. With an ITO thickness of 50 nm (140 nm respectively), the optimal structure consists of a 200 nm thick organic layer and a 300 nm thick SiO₂ layer. The resulting effective index contrast $\Delta_{neff} = 0.061$ ($\Delta_{neff} = 0.075$ respectively) is much smaller than when the bulk indices are used ($\Delta_{neff} = 0.25$). On the basis of the optimal effective indices, the width of the high-effective index lines is $\Lambda_1 = 95$ nm, and the width of the low-effective index spacing is $\Lambda_2 = 99$ nm.

In the third step, also conducted using the transfer-matrix formalism, the width of the mirror reflectance (forbidden bandgap) is maximized so as to cover the largest part of the electroluminescence spectrum of the chosen organic material. This study predicts

that with the better effective index contrast ($\Delta_{neff} = 0.061$), the mirror offers a $\Delta\lambda = 20$ nm FWHM reflectance.

In the fourth step, the conditions of the number of grating periods to maximize the quality factors are identified. To achieve quality factors above 3000, at least $N \geqslant 66$ periods of the grating are necessary. When taking into account the absorption, an optimal micro-cavity consists of a first-order DFB mirror made with $N = 80$ periods separated by a second-order DFB grating made of M (<10) periods plus one ending line.

Before integrating the cavity into an OLED and investigating a full device, we fabricated and validated different DFB micro-cavities by investigating their ability to achieve lasing under optical pumping. On a glass substrate covered with 300 nm of SiO_2 and 140 nm of ITO, we patterned a matrix of different DFB cavities via e-beam lithography. These matrices are made with three sections of mixed-order DFB cavities with different grating periods and different e-beam doses. Once patterned, the cavities are covered with the organic gain medium made of 200 nm of Alq3 doped at 2% with DCM. The cavities are then optically pumped with a 355 nm laser, and their light emissions are measured for different pump intensities. Lasing was observed for a limited number of DFB-cavity geometries and doses, notably, those made with $l_{1L} = 112$ nm, $l_{1H} = 96$ nm and a dose of 700 $\mu C/cm^2$ resulting in an emission of $\lambda_R = 627$ nm and a laser threshold of 125.4 $\mu J/cm^2$.

These results give credence to the notion that an organic laser diode can be achieved through the integration of this cavity with an organic heterostructure and electrical excitation. The proposed method paves the way for further improvement in the cavity design to reduce laser thresholds. Furthermore, we observed that there is a systematic deviation of the observed resonance wavelength from the nominal Bragg wavelength. The 5% averaged deviation cannot be attributed solely to geometric uncertainties induced by the fabrication, but also to the uncertainties in the refractive index—which highlight the necessity for DFB cavity design—and to the consideration of the calculated effective indices rather than the bulk indices.

As a perspective, we will study a mixed-order cavity structured with a 50 nm thick ITO layer, a 300 nm thick SiO_2 layer, and a 200 nm thick organic layer, offering a larger confinement factor and a larger index contrast.

To bring the technology to maturity, we envisioned a five-step roadmap, the first being partially completed: The first step deals with intense electrical excitation at the level of tens of kA/cm^2 to reach the laser threshold. This step has been reached under nanosecond-pulsed electrical excitation [22]. The second step deals with the design and the fabrication of high-quality factor cavities compatible with thin-film organic semiconductors, which is the subject of the current work. The third step is to identify among the many organic semiconductors laser gain media those offering the optimal net gain, that is, the optimum gain minus loss. This step was partially addressed by the publication of a calculation criterion for re-absorption allowing for the comparison of materials between them [23]. This criterion has yet to be used to compare materials, however. It is very likely that other sources of material losses, such as triplet absorption, have to be better understood. The fourth step deals with the design of material strategies to manage losses, including triplet losses such that CW operation of the laser is possible. The fifth step deals with study of the reliability of the organic laser diodes, including photobleaching.

Institutional Review Board Statement: Not applicable.

Informed Consent Statement: Not applicable.

Data Availability Statement: Not applicable.

Conflicts of Interest: The authors declare no conflict of interest.

References

1. Yoshida, K.; Manousiadis, P.P.; Bian, R.; Chen, Z.; Murawski, C.; Gather, M.C.; Haas, H.; Turnbull, G.A.; Samuel, I.D.W. 245 MHz bandwidth organic light-emitting diodes used in a gigabit optical wireless data link. *Nat. Commun.* **2020**, *11*, 1171. [CrossRef] [PubMed]

2. Fitzner, R.; Mena-Osteritz, E.; Mishra, A.; Schulz, G.; Reinold, E.; Weil, M.; Körner, C.; Ziehlke, H.; Elschner, C.; Leo, K.; et al. Correlation of π-Conjugated Oligomer Structure with Film Morphology and Organic Solar Cell Performance. *J. Am. Chem. Soc.* **2012**, *134*, 11064–11067. [CrossRef] [PubMed]

3. Lee, K.-H.; Leem, D.-S.; Sul, S.; Park, K.-B.; Lim, S.-J.; Han, H.; Kim, K.-S.; Jin, Y.W.; Lee, S.; Park, S.Y. A high-performance greensensitive organic photodiode comprising a bulk heterojunction of dimethyl-quinacridone and dicyanovinyl terthiophene. *J. Mater. Chem. C* **2013**, *1*, 2666. [CrossRef]

4. Herrnsdorf, J.; Guilhabert, B.; Chen, Y.; Kanibolotsky, A.L.; Mackintosh, A.R.; Pethrick, R.A.; Skabara, P.J.; Gu, E.; Laurand, N.; Dawson, M.D. Flexible blue-emitting encapsulated organic semiconductor DFB laser. *Opt. Express* **2010**, *18*, 25535–25545. [CrossRef] [PubMed]

5. Yang, Y.; Turnbull, G.A.; Samuel, D.W. Sensitive Explosive Vapor Detection with Polyfluorene Lasers. *Adv. Funct. Mater.* **2010**, *20*, 2093–2097. [CrossRef]

6. *OLED Microdisplays: Technology and Applications*; Templier, F. (Ed.) John Wiley & Sons: Hoboken, NJ, USA, 2014; ISBN 9781848215757. [CrossRef]

7. Templier, F. GaN-based emissive microdisplays: A very promising technology for compact, ultra-high brightness display systems. *J. Soc. Inf. Disp.* **2016**, *24*, 669–675. [CrossRef]

8. Pope, M.; Swenberg, C.E. *Electronic Processes in Organic Crystals and Polymers*; Oxford University Press: New York, NY, USA, 1999.

9. Karnutsch, C.; Pflumm, C.; Heliotis, G.; Demello, J.C.; Bradley, D.D.; Wang, J.; Weimann, T.; Haug, V.; Gärtner, C.; Lemmer, U. Improved organic semiconductor lasers based on a mixed-order distributed feedback resonator design. *Appl. Phys. Lett.* **2007**, *90*, 131104. [CrossRef]

10. Karnutsch, C.; Gýrtner, C.; Haug, V.; Lemmer, U.; Farrell, T.; Nehls, B.S.; Scherf, U.; Wang, J.; Weimann, T.; Heliotis, G.; et al. Low threshold blue conjugated polymer lasers with first- and second-order distributed feedback. *Appl. Phys. Lett.* **2006**, *89*, 201108. [CrossRef]

11. Namdas, E.B.; Tong, M.; Ledochowitsch, P.; Mednick, S.R.; Yuen, J.D.; Moses, D.; Heeger, A.J. Low Thresholds in Polymer Lasers on Conductive Substrates by Distributed Feedback Nanoimprinting: Progress Toward Electrically Pumped Plastic Lasers. *Adv. Mater.* **2009**, *21*, 799–802. [CrossRef]

12. Hirade, M.; Nakanotani, H.; Hattori, R.; Ikeda, A.; Yahiro, M.; Adachi, C. Low-Threshold Blue Emission from First-Order Organic DFB Laser Using 2,7-bis[4-(N-carbazole)phenylvinyl]-9,9′-Spirobifluorene as Active Gain Medium. *Mol. Cryst. Liq. Cryst.* **2009**, *504*, 1–8. [CrossRef]

13. Xia, R.; Lai, W.Y.; Levermore, P.A.; Huang, W.; Bradley, D.D. Low-Threshold Distributed-Feedback Lasers Based on Pyrene-Cored Starburst Molecules with 1,3,6,8-Attached Oligo(9,9-Dialkylfluorene) Arms. *Adv. Funct. Mater.* **2009**, *19*, 2844–2850. [CrossRef]

14. Sandanayaka, A.S.; Matsushima, T.; Bencheikh, F.; Terakawa, S.; Potscavage, W.J.; Qin, C.; Fujihara, T.; Goushi, K.; Ribierre, J.C.; Adachi, C. Indication of current-injection lasing from an organic semiconductor. *Appl. Phys. Express* **2019**, *12*, 061010. [CrossRef]

15. Sandanayaka, A.S.; Matsushima, T.; Bencheikh, F.; Terakawa, S.; Potscavage, W.J.; Qin, C.; Fujihara, T.; Goushi, K.; Ribierre, J.C.; Adachi, C. Amplified spontaneous emission in an organic semiconductor multilayer waveguide structure including a highly conductive transparent electrode. *Appl. Phys. Lett.* **2005**, *86*, 221102. [CrossRef]

16. Available online: htttps://www.computational-photonics.eu (accessed on 10 February 2020).

17. Coens, A.; Chakaroun, M.; Fischer, A.P.A.; Lee, M.W.; Boudrioua, A.; Geffroy, B.; Vemuri, G. Experimental optimization of the optical and electrical properties of a half-wavelength-thick organic hetero-structure in a Micro-cavity. *Opt. Express* **2012**, *20*, 29252–29259. [CrossRef] [PubMed]

18. Brütting, W.; Berleb, S.; Mückl, A.G. Device Physics of Organix Light-Emitting Diodes Based on Molecular Materials. *Org. Electron.* **2001**, *2*, 1–36. [CrossRef]

19. Chakaroun, M.; Coens, A.; Fabre, N.; Gourdon, F.; Solard, J.; Fischer, A.; Boudrioua, A.; Lee, C.C. Optimal design of a microcavity organic laser device under electrical pumping. *Opt. Express* **2011**, *19*, 493. [CrossRef] [PubMed]

20. Birch, D.J.S.; Hungerford, G.; Imhof, R.E.; Holmes, A.S. The fluorescence properties of DCM. *Chem. Phys. Lett.* **1991**, *178*, 177–184. [CrossRef]

21. Al-Kaysi, R.O.; Ahn, T.S.; Müller, A.M.; Bardeen, C.J. The photophysical properties of chromophores at high (100 mM and above) concentrations in polymers and as neat solids. *Phys. Chem. Chem. Phys.* **2006**, *8*, 3453–3459. [CrossRef]
22. Ouirimi, A.; Chime, A.C.; Loganathan, N.; Chakaroun, M.; Fischer, A.P.A.; Lenstra, D. Threshold estimation of an organic laser diode using a rate-equation model validated experimentally with a microcavity OLED submitted to nanosecond electrical pulses. *Org. Electron.* **2021**, *97*, 106190. [CrossRef]
23. Lenstra, D.; Fischer, A.P.A.; Ouirimi, A.; Chime, A.C.; Loganathan, N.; Chakaroun, M. Organic Diode Laser Dynamics: Rate-Equation Model, Reabsorption, Validation and Threshold Predictions. *Photonics* **2021**, *8*, 279. [CrossRef]